Title: State-dependence of CO_2 Forcing and its Implications for Climate Sensitivity

Authors: Haozhe He[1]*, Ryan J. Kramer[2,3], Brian J. Soden[1], Nadir Jeevanjee[4]

Affiliations:

[1]Rosenstiel School of Marine, Atmospheric and Earth Science, University of Miami, Miami, FL, USA.

[2]Goddard Earth Science Technology and Research II, University of Maryland at Baltimore County, Baltimore MD, USA.

[3]Climate and Radiation Laboratory, NASA Goddard Space Flight Center, Greenbelt, MD, USA.

[4]Geophysical Fluid Dynamics Laboratory, Princeton, NJ, USA.

*Corresponding author. Email: haozhe.he@miami.edu

Abstract: When evaluating the effect of CO_2 changes on the earth's climate, it is widely assumed that instantaneous radiative forcing from a doubling of a given CO_2 concentration ($IRF_{2\times CO2}$) is constant and that variances in climate sensitivity arise from differences in radiative feedbacks, or dependence of these feedbacks on the climatological base-state. In this paper, we show that the $IRF_{2\times CO2}$ is not constant, but also depends on the climatological base-state, increasing by ~25% for every doubling of CO_2, and has increased by ~10% since the pre-industrial era primarily due to the cooling within the upper stratosphere, implying a proportionate increase in climate sensitivity. This base-state dependence also explains about half of the intermodel spread in $IRF_{2\times CO2}$, a problem that has persisted among climate models for nearly three decades.

One-Sentence Summary: Carbon dioxide becomes a more potent greenhouse gas as the climate changes in response to increased carbon dioxide.

Main Text: Radiative forcing (RF) refers to a change in net radiative flux at the top-of-atmosphere (TOA) due to an externally-imposed perturbation in the earth's energy balance (*1, 2*), such as anthropogenic activities (e.g., emission of greenhouse gases and aerosols) or natural events (e.g., volcanic eruptions). The earth subsequently warms or cools to counteract the flux perturbation and restore radiative equilibrium. The RF is commonly separated into two parts (*1, 3–6*): instantaneous radiative forcing (IRF), which measures the change in net radiative flux that results only from the change in forcing agents, and rapid adjustments, which consist of radiative perturbations induced by atmospheric responses to the IRF independent of any change in surface temperature. This study focuses on the IRF, considered to be the best-understood aspect of RF (*7*). For CO_2 perturbations, the IRF is responsible for approximately two-thirds of the total RF and is the fundamental driver of the rapid adjustments (*1, 3–6, 8–12*), wherein stratospheric cooling is the dominant adjustment to CO_2 forcing (*11, 12*). However, several previous studies have shown that the IRF from a doubling of CO_2 concentration ($IRF_{2\times CO2}$) varies by ~50% among climate models (*10, 13–15*). Although this spread has persisted for nearly three decades, its underlying cause has never been fully resolved.

Climate sensitivity is formally defined as the change in global-mean surface temperature required to restore radiative equilibrium in response to a doubling of CO_2 concentration ($\Delta T_{2\times CO2}$) and is the most widely used metric to quantify the susceptibility of the climate to an externally forced change, i.e., $\Delta T_{2\times CO2} = -RF_{2\times CO2}/\lambda$, where the radiative damping (λ in W m^{-2} K^{-1}) is the efficiency at which radiative equilibrium is restored per unit change in surface temperature. The radiative damping depends on a number of well and not-so-well understood feedbacks within the climate system, and is widely recognized to both vary between climate models and vary in time as the climatological base-state evolves. However, the intermodel variance in the $RF_{2\times CO2}$ and its dependence on the base-state are less well recognized. In this study, we demonstrate that the $IRF_{2\times CO2}$ is not a constant, but also depends on the climatological base-state, as suggested by a recent analytical model (*16*). This state-dependence not only explains about half of the intermodel variance in $IRF_{2\times CO2}$, but fundamentally reshapes our understanding of climate sensitivity with significant implications for both past and future climate changes.

Results

The Coupled Model Intercomparison Projects (CMIP), provide a series of coordinated experiments performed in support of the IPCC assessments in which model simulations are achieved using identical emission scenarios (*17, 18*). However, because determining the IRF requires additional calculations, it is not routinely computed for most experiments. In the first comprehensive RF comparison among climate models, Cess et al. (*13*) found that the $IRF_{2\times CO2}$ ranged from roughly 3.3 to 4.7 W m^{-2}. Subsequent studies with newer generations of models found a similar range (10, *14*). This spread was thought to mainly arise from intermodel differences in the parameterization of infrared absorption by CO_2 (*15*).

Double-call radiative transfer calculations are the most direct method for diagnosing the IRF in model simulations. To produce these specialized online diagnostics, a second call is made to the radiation scheme at each timestep. Radiative fluxes are re-calculated with a hypothetical forcing agent perturbation, such as CO_2 at some increased concentration. These perturbations are solely used to diagnose the IRF and do not interact with the model simulation. Although only a few online double-call calculations were performed by climate models from CMIP5/6, the available output is particularly useful for investigating the state-dependence of CO_2 IRF. To avoid the complicating effects of clouds in masking the IRF (*7, 19, 20*), we further simplify our analysis by limiting it to infrared CO_2 forcing at the TOA under clear-sky conditions.

Figure 1A shows the *online* double-call calculations available from CMIP5/6 models for the historical AMIP experiment, which contains the most online double-call calculations of any of the CMIP experiments (12 out of 80 participating models provided calculations for this experiment; Tables S1 and S2). The amip experiment consists of atmosphere-only model simulations that all use identical, time-varying sea surface temperatures observed over the period 1979–2008 as boundary conditions. The online double-calls provided are for 4×CO2; note that $IRF_{4\times CO2} \approx 2\times IRF_{2\times CO2}$ for a given climate state (see Materials and Methods). The results exhibit a large intermodel spread (ranging from ~4 to 8 W m^{-2}), consistent with that observed in previous model generations (*15*).

To investigate the extent to which differences in the thermal structure of the climatological base-state can explain the intermodel spread of IRF, we perform *offline* double-call $IRF_{4\times CO2}$ calculations using original atmospheric profiles from the AMIP models and a single radiative transfer model (SOCRATES; see Materials and Methods). In contrast to the *online* counterparts, the same radiative transfer parameterization is used in all of the offline calculations, so their inter-model spread is only due to differences in the climatological base-states. The strong correlation (r=0.82) between the IRFs from the online and offline double-call calculations (Fig. 1B) suggests that more than half of the intermodel variance in $IRF_{4\times CO2}$ results from differences in climatological base-states, not differences in representing the spectral absorption of CO_2. This is consistent with a recent study by Pincus et al. (*19*), who computed IRF from different radiative transfer schemes but using the same climatological base-state and found a much smaller spread in $IRF_{4\times CO2}$ than in the online double-calls (Fig. 1A). Together, these studies provide compelling evidence to suggest that intermodel differences in the climatological base-state are an essential contributor to the spread in CO_2 IRF.

The influence of the base-state on CO_2 IRF is more clearly illustrated in the coupled model simulations from CMIP6 in which a 1% per year increase is imposed in the atmospheric CO_2 concentration (1pctCO2; Fig. 2). Although only two models (solid lines in Fig. 2A) submitted online double-call calculations, the results reveal a dramatic growth in $IRF_{4\times CO2}$ as the climatological base-state evolves. For both models, $IRF_{4\times CO2}$ increases from ~5 W m^{-2} when $IRF_{4\times CO2}$ is computed in a pre-industrial climate to ~8 W m^{-2} when it is computed in an elevated-CO_2 climate. This challenges the widely held assumption that the $IRF_{2\times CO2}$ is constant (*21*–*23*). To the contrary, it demonstrates that the CO_2 IRF is a dynamic quantity that changes substantially as the climate changes.

To verify this result, we perform a series of line-by-line and SOCRATES offline double-call calculations using the full suite of CMIP5/6 coupled simulations under the 1pctCO2 scenario (Fig. 2A, markers). These results both confirm the dramatic increase in $IRF_{4\times CO2}$ using a much larger ensemble of models and, since the same radiative transfer scheme is used for all offline calculations, indicate that changes in the climatological base-state are responsible for this increase. Note that the climatological base-state here includes the thermal structure as well as the base-state CO_2 concentration (*24*–*26*), both of which vary with each timestep. However, most of the $IRF_{4\times CO2}$ increases are due to the evolution of thermal structure, especially for the first doubling of base-state CO_2 concentration (Fig. S1).

According to the analytical model of Jeevanjee et al. (*16*), the dependence of CO_2 IRF on the climatological base-state can be understood in terms of dependence on the emission temperature of both stratosphere and troposphere as follows:

$$\mathcal{F} = 2l \ln\left(\frac{q_f}{q_i}\right)[\pi B(\nu_0, \bar{T}_{em}) - \pi B(\nu_0, T_{strat})]$$

where l is the 'spectroscopic decay' parameter of 10.2 cm^{-1}, q_i is the initial CO_2 concentration, q_f is the final CO_2 concentration, and $\pi B(\nu_0, \bar{T}_{em} \,/\, T_{strat})$ is the hemispherically integrated Planck function at peak absorption wavenumber of CO_2 with either the tropospheric emission temperature or stratospheric emission temperature (see Materials and Methods). The latter refers to the temperature of the upper stratosphere, where unit optical depth is achieved by the peak of the CO_2 absorption band, while the former depends on surface temperature and free-troposphere relative humidity. This model has been used to help explain the spatially inhomogeneous distribution of IRF that results from a spatially uniform increase of CO_2 (*27*).

As CO_2 increases in the 1pctCO2 simulations, the surface temperature warms, and the stratosphere cools roughly linearly over time (Figs. 2B and 2C). To assess the relative contributions of these changes in climate to the increase in $IRF_{4\times CO2}$, we include results from the CMIP6 abrupt-4×CO2 experiment (Fig. 2, dashed lines; only one model provided online double-call calculations for this experiment). In contrast to the 1pctCO2 experiment, CO_2 is instantly quadrupled in the abrupt-4×CO2 experiment causing the surface to warm rapidly over the first few decades before leveling off. The stratosphere adjusts even more rapidly, equilibrating to a new temperature within the first year.

The contrasting temporal evolution of the climate between these two scenarios is reflected in the $IRF_{4\times CO2}$. For instance, the $IRF_{4\times CO2}$ with abrupt-4×CO2 base-state exhibits only a mild increase with global-mean surface warming (Fig. 2), indicating a relatively weak dependence of the CO_2 IRF on surface temperature. In contrast, $IRF_{4\times CO2}$ in the 1pctCO2 experiment exhibits a much larger increase over time, despite having a similar change in global-mean surface temperature. Physically, the CO_2 IRF represents a swap of tropospheric emission for stratospheric emission (*16*), and since the temperature change within the stratosphere is much larger than that at the surface and within the troposphere, the IRF increase closely follows the stratosphere cooling, suggesting a dominant role of stratospheric temperature on the CO_2 IRF. We emphasize that the results in Fig. 2A represent IRF only and do not include the stratospheric adjustment. Rather the changes in IRF over time reflect the impact of the stratospheric adjustment from prior CO_2 changes on the base-state which, in turn, amplifies the IRF that would result from a subsequent "hypothetical" quadrupling of CO_2. As cloud masking has virtually no influence on stratospheric emission, the dominant role of stratospheric temperature also remains under all-sky conditions.

The state-dependence of CO_2 IRF on the surface temperature and stratospheric temperature is also evident in the amip simulations (Fig. 1A). Since these simulations adopt the same sea surface temperature as their boundary conditions, our results imply that differences in stratospheric temperature are primarily responsible for the intermodel spread in $IRF_{4\times CO2}$. To confirm the role of the stratospheric temperature on the IRF spread, we also perform the SOCRATES offline double-call IRF calculations using the same amip base-states and check its correlation with the corresponding air temperature at 10 hPa, which is the highest level of CMIP5 standard pressure-level outputs [and is closest to the level with unit optical depth achieved by the peak of the CO_2 absorption band (*16, 20, 28*)]. A high, significant correlation is found between the IRF and stratospheric temperature across both CMIP6 and CMIP5 models (Figs. 1C and S2), highlighting that biases in stratospheric temperature play a dominant role in causing the intermodel spread in CO_2 IRF.

The overwhelming role of stratospheric temperature over surface temperature is also reflected in the brief declines for many models in the magnitude of the $IRF_{4\times CO2}$ in the year 1992, following the eruption of Mount Pinatubo (Fig. 1A). On average across the models there was only a 0.2 K surface temperature decrease but a ~1 K temperature increase at 10 hPa in 1992 compared to 1991.

The analytical model of CO_2 IRF by Jeevanjee et al. (*16*) replicates the offline double-call $IRF_{4\times CO2}$ of CMIP6 and CMIP5 with high correlations for abrupt-4×CO2 simulations (Figs. 3A and S3), providing a computationally efficient alternative for investigating the sensitivity of the CO_2 IRF to stratospheric temperatures. Since the 10 hPa temperatures cool at a similar rate for all models under 1pctCO2 scenarios from CMIP6 and CMIP5 (Figs. 3B and S4), the temperatures at this level have nearly identical intermodel spread at the beginning and the end of the simulations. This suggests that intermodel spread in the CO_2 IRF arises explicitly from differences in the initial stratospheric temperatures under pre-industrial conditions. We confirm this with the analytical model, finding it produces the same IRF intermodel spread, highly correlated with the offline double-call calculations, even when the initial, pre-industrial upper stratospheric temperatures are used as input for every timestep instead of the actual, time-varying temperature from the corresponding abrupt-4×CO2 simulations (Figs. 3C and S5).

Briefly, our results demonstrate that CO_2 IRF increases as the climate changes in response to increased CO_2. Online and offline double-call calculations from the CMIP6 historical simulations (Figs. 4A and S6A as well as Table S3) indicate that $IRF_{4\times CO2}$ is about 10% larger today than it was in the mid-19th century due to the change in base-state, primarily from stratospheric cooling. This amplification arises predominantly from the increase in well-mixed greenhouse gases over this period (Fig. 4A). Thus, the $IRF_{4\times CO2}$ increases over time because the CO_2-induced cooling of the stratosphere makes any subsequent change in CO_2 more potent.

Since it is the sum of the IRF and rapid adjustments, known as the total or "effective" RF, that ultimately drives climate change (*1, 3, 4, 29*), it is important to understand the extent to which the rapid adjustments may also depend on the base-state. To investigate the state-dependence of the adjustments, we use atmosphere-only model simulations forced by boundary conditions of both the preindustrial era (piclim-control) and recent decades (amip), along with their corresponding 4×CO2 counterparts (piclim-4×CO2 and amip-4×CO2; see Materials and Methods as well as Table S4). The amip simulation not only has a higher prescribed CO_2 concentration than that of the piclim-control simulation, but also has cooler stratosphere temperature, allowing us to quantify the magnitude of the adjustments under two different base-states.

The stratospheric adjustment is the most important of the rapid adjustments to CO_2 forcing, typically an order of magnitude larger than tropospheric adjustments (*11, 12*). The sum of IRF and stratospheric adjustment, or the "stratospheric adjusted" RF, are roughly equal at the tropopause and the TOA (*30*) and provides an accurate and computationally efficient analog for the total RF. Figure S6 compares the IRF, stratospheric adjustments, and stratospheric adjusted RF from the CO_2 quadrupling for the two different base-states (see Materials and Methods). The amip simulations exhibit a larger IRF (Fig. S6A; 0.38 W m^{-2}) compared to that obtained under preindustrial conditions due to the cooler stratosphere. There is a nearly identical difference in the stratospheric adjusted RF between the two sets of experiments (Fig. S6C; 0.34 W m^{-2}), because almost no difference is seen in the stratospheric adjustments (Fig. S6B; –0.03 W m^{-2}). Note that the abovementioned ensemble-mean forcing differences are also corroborated by differences shown for individual models. Even though the direct contribution of the base-state to the inter-model spread in stratospheric adjusted RF and total RF is smaller than it is for the IRF, as additional

sources of spread contribute, we note there are high, significant correlations between the IRF and both the stratospheric adjusted RF and total RF (Figs. S7A & S7B).

The state-dependence of both the IRF and stratospheric adjustment is further explored using the more realistic, online, interactive, coupled simulations, forced by abruptly halving, doubling, and quadrupling CO_2 concentration of the preindustrial era (abrupt-0.5×CO2, abrupt-2×CO2, and abrupt-4×CO2; see Materials and Methods as well as Table S5), respectively. As expected, for every model analyzed we find that the IRF grows in magnitude across the three sets of experiments, for each successive CO_2 doubling (Fig. S8). The stratospheric adjusted RF exhibits a nearly identical increase across the experiments, with the stratospheric adjustment only weakly offsetting the increases. Similar increases per CO_2 doubling have also been found for the total RF, estimated from atmosphere-only simulations with fixed sea surface temperatures (*31*). This indicates that, with almost no counteracting effects from rapid adjustments, the radiative effects from the stratospheric temperature base-state dependence of the IRF extend to the total RF (Figs. S6–S8) and thus on to climate sensitivity.

Changes in climate sensitivity can therefore arise from both changes in climate feedbacks as well as changes in IRF. More generally, these results indicate that, despite the logarithmic dependence of CO_2 absorption (*28*), the climate becomes increasingly sensitive to a doubling of CO_2, as the base-state CO_2 concentration increases and the stratosphere cools correspondingly. The $IRF_{2\times CO2}$ increases by ~25% for each doubling of base-state CO_2 concentration (the $IRF_{2\times CO2}$ increases by 24% and 29% for the first and second doubling of base-state CO_2 concentration, respectively; Fig. 2A). Since the IRF accounts for roughly two-thirds of the total RF from CO_2 (*1, 10–12*), this implies that $\Delta T_{2\times CO2}$ increases by ~15–20% for each doubling of CO_2 just due to changes in the IRF. This state-dependence of the $IRF_{2\times CO2}$, and thus $\Delta T_{2\times CO2}$, has not been accounted for in the latest IPCC reports.

Potential climate implications

Since the upper stratospheric temperature plays a dominant role in determining the magnitude of the CO_2 IRF, any changes in atmospheric composition that perturb stratospheric temperature could subsequently impact the climate. Consider the recent example of polar ozone depletion (*32–34*), which strongly influences the temperature structure within the stratosphere (*35*). The ozone depletion since the 1970s has led to strong cooling within the stratosphere. By cooling the stratosphere, ozone depletion makes the forcing from the increase in CO_2 over this period more potent. Note that although the stratospheric ozone loss mainly occurs in the lower stratosphere (*36, 37*), the associated cooling also contributes to a decline in infrared emission from the lower to the upper stratosphere, thus strengthening the CO_2 IRF at the TOA.

Here, we examine this nonlinear interaction between ozone depletion-induced cooling and CO_2 IRF by comparing a 10-member ensemble of model simulations that use all historical forcings with the corresponding sum of model simulations in which each historical forcing is imposed independently (see Materials and Methods). According to our theory, model simulations in which ozone loss and CO_2 increase coincide should have a larger CO_2 forcing (and greater surface warming) than the sum of individual model simulations in which each forcing is imposed separately in isolation from the other. The CO_2 forcing in the latter is smaller because it is not enhanced by ozone depletion-induced cooling. We compute the indirect surface warming effect of ozone depletion by taking the ensemble-mean difference in surface temperature anomalies between these two sets of experiments averaged over the period 1985–2014 (see Materials and Methods).

As predicted, the sign and spatial distribution of the nonlinear contribution of ozone loss to CO_2 IRF is consistent with a base-state dependence of IRF (Fig. 4B). Most of the indirect surface warming effect occurs around the poles, where the local stratosphere has the strongest cooling, although some heat transport may also be playing a role (*38, 39*). The smaller warming over the southern high latitudes likely reflects the greater rate of ocean heat uptake by the Southern Ocean (*40, 41*). This supports the premise that any forcing agent changes that perturb the stratospheric temperature could also impact the climate by modulating the CO_2 IRF at the TOA, even without changing the CO_2 amount.

Our findings may also help to better understand past climate events, such as the end-Devonian mass extinction and the Paleoproterozoic "snowball earth" conditions, occurred following similar but considerably stronger perturbations, i.e., a dramatic drop in stratosphere ozone (*42*) and the inevitable development of an ozone layer (*43, 44*), respectively. The base-state dependence of the CO_2 IRF may have implications for how other related metrics are defined, such as global warming potential and efficacy of non-CO_2 forcing (*9, 29*), since they are quantified relative to the radiative effects of a CO_2 perturbation. These metrics are often used in policy discussions, so it will be particularly important to determine if they must be re-defined with consideration of the dynamic (i.e., non-constant) behavior of CO_2 IRF.

Additionally, our results may have implications for geoengineering and climate change mitigation (*45*). Taking 1992 - the year following the 1991 eruption of Mount Pinatubo - as an example, the injected volcanic aerosols within the stratosphere not only cooled the surface by reflecting more solar radiation back to the space but also warmed the stratosphere by increasing the atmospheric absorption of sunlight in the stratosphere (*46, 47*). The resulting stratospheric warming weakened the CO_2 IRF (Figs. 1A and 4A) and reduced the warming efficacy of CO_2. As most geoengineering approaches involving stratospheric aerosol injection employ reflective aerosols [e.g., sulfate (*48*)], alternative approaches that use more absorbing aerosols (e.g., black carbon) may warrant consideration, as it could effectively reduce the CO_2 greenhouse effect by warming the upper stratosphere (Fig. S9) (*49, 50*).

Lastly, we note that the model simulations of stratospheric temperature can be easily constrained with observations. Across multiple sets of observations and reanalyses (see Materials and Methods as well as Table S6), the global- and annual-mean 10 hPa air temperature has an uncertainty range of 226.6 to 228.4 K in the year 2020. This ~1.8 K difference in base-state would translate to only a ~0.16 (0.18) W m^{-2} $IRF_{4\times CO2}$ uncertainty for CMIP6 (CMIP5) models (Figs. 1C and S2). This highlights the importance of accurately representing the stratosphere when projecting future CO_2-induced climate change and the potential to better constrain model projections using observations, further emphasizing the importance of continuing observations in Earth's middle and upper atmosphere (*51*).

References

1. G. Myhre, D. Shindell, F.-M. Bréon, W. Collins, J. Fuglestvedt, J. Huang, D. Koch, J.-F. Lamarque, D. Lee, B. Mendoza, T. Nakajima, A. Robock, G. Stephens, T. Takemura, H. Zhang, "[Anthropogenic and Natural Radiative Forcing]" in Climate Change 2013 - The Physical Science Basis. Contribution of Working Group I to the Fifth Assessment Report of the Intergovernmental Panel on Climate Change (Cambridge University Press, Cambridge, United Kingdom and New York, NY, USA, 2009), pp. 659–740.

2. R. J. Kramer, H. He, B. J. Soden, L. Oreopoulos, G. Myhre, P. M. Forster, C. J. Smith, Observational evidence of increasing global radiative forcing. *Geophys. Res. Lett.* **48**, e2020GL091585 (2021). https://doi.org/10.1029/2020GL091585

3. O. Boucher, D. Randall, P. Artaxo, C. Bretherton, G. Feingold, P. Forster, V.-M. Kerminen, Y. Kondo, H. Liao, U. Lohmann, P. Rasch, S.K. Satheesh, S. Sherwood, B. Stevens X.Y. Zhang, "[Clouds and Aerosols]" in Climate Change 2013 - The Physical Science Basis. Contribution of Working Group I to the Fifth Assessment Report of the Intergovernmental Panel on Climate Change (Cambridge University Press, Cambridge, United Kingdom and New York, NY, USA, 2009), pp. 659–740.

4. S. C. Sherwood, S. Bony, O. Boucher, C. Bretherton, P. M. Forster, J. M. Gregory, B. Stevens, Adjustments in the Forcing-Feedback Framework for Understanding Climate Change. *B. Am. Meteorol. Soc*. **96**, 217–228 (2015). https://doi.org/10.1175/BAMS-D-13-00167.1

5. P. M. Forster, T. Richardson, A. C. Maycock, C. J. Smith, B. H. Samset, G. Myhre, T. Andrews, R. Pincus, M. Schulz, Recommendations for diagnosing effective radiative forcing from climate models for CMIP6. *J. Geophys. Res. Atmospheres* **121**, 12,460–12,475 (2016). https://doi.org/10.1002/2016JD025320

6. V. Ramaswamy, W. Collins, J. Haywood, J. Lean, N. Mahowald, G. Myhre, V. Naik, K. P. Shine, B. Soden, G. Stenchikov, T. Storelvmo, Radiative forcing of climate: the historical evolution of the radiative forcing concept, the forcing agents and their quantification, and applications. *Meteor. Mon*. **59**, 14.1–14.101 (2019). https://doi.org/10.1175/AMSMONOGRAPHS-D-19-0001.1

7. M. G. Mlynczak, T. S. Daniels, D. P. Kratz, D. R. Feldman, W. D. Collins, E. J. Mlawer, M. J. Alvarado, J. E. Lawler, L. W. Anderson, D. W. Fahey, L. A. Hunt, J. C. Mast, The spectroscopic foundation of radiative forcing of climate by carbon dioxide. *Geophys. Res. Lett.* **43**(10), 5318–5325 (2016). https://doi.org/10.1002/2016GL068837

8. K. P. Shine, J. Cook, E. J. Highwood, M. M. Joshi, An alternative to radiative forcing for estimating the relative importance of climate change mechanisms. *Geophys. Res. Lett.* **30**(20), 2047 (2003). https://doi.org/10.1029/2003GL018141

9. J. Hansen, M. Sato, R. Ruedy, L. Nazarenko, A. Lacis, G. A. Schmidt, G. Russell, I. Aleinov, M. Bauer, S. Bauer, N. Bell, B. Cairns, V. Canuto, M. Chandler, Y. Cheng, A. D. Genio, G. Faluvegi, E. Fleming, A. Friend, T. Hall, C. Jackman, M. Kelley, N. Kiang, D. Koch, J. Lean, J. Lerner, K. Lo, S. Menon, R. Miller, P. Minnis, T. Novakov, V. Oinas, Ja. Perlwitz, Ju. Perlwitz, D. Rind, A. Romanou, D. Shindell, P. Stone, S. Sun, N. Tausnev, D. Thresher, B. Wielicki, T. Wong, M. Yao, S. Zhang, Efficacy of climate forcings. *J. Geophys. Res. Atmospheres* **110**, D18104 (2005). https://doi.org/10.1029/2005JD005776

10. E.-S. Chung, B. J. Soden, An assessment of methods for computing radiative forcing in climate models. *Environ. Res. Lett.* **10**, 074004 (2015). https://doi.org/10.1088/1748-9326/10/7/074004

11. C. J. Smith, R. J. Kramer, G. Myhre, P. M. Forster, B. J. Soden, T. Andrews, O. Boucher, G. Faluvegi, D. Fläschner, Ø. Hodnebrog, M. Kasoar, V. Kharin, A. Kirkevåg, J. -F. Lamarque, J. Mülmenstädt, D. Olivié, T. Richardson, B. H. Samset, D. Shindell, P. Stier, T. Takemura, A. Voulgarakis, D. Watson-Parris, Understanding rapid adjustments to diverse forcing

agents. *Geophys. Res. Lett.* **45**, 12,023–12,031 (2018). https://doi.org/10.1029/2018GL079826

12. C. J. Smith, R. J. Kramer, G. Myhre, K. Alterskjær, W. Collins, A. Sima, O. Boucher, J.-L. Dufresne, P. Nabat, M. Michou, S. Yukimoto, J. Cole, D. Paynter, H. Shiogama, F. M. O'Connor, E. Robertson, A. Wiltshire, T. Andrews, C. Hannay, R. Miller, L. Nazarenko, A. Kirkevåg, D. Olivié, S. Fiedler, R. Pincus, P. M. Forster, Effective radiative forcing and adjustments in CMIP6 models. *Atmospheric Chem. Phys.* **20**, 9591–9618 (2020). https://doi.org/10.5194/acp-20-9591-2020

13. R. D. Cess, M.-H. Zhang, G. L. Potter, H. W. Barker, R. A. Colman, D. A. Dazlich, A. D. D. Genio, M. Esch, J. R. Fraser, V. Galin, W. L. Gates, J. J. Hack, W. J. Ingram, J. T. Kiehl, A. A. Lacis, H. L. Treut, Z.-X. Li, X.-Z. Liang, J.-F. Mahfouf, B. J. McAvaney, V. P. Meleshko, J.-J. Morcrette, D. A. Randall, E. Roeckner, J.-F. Royer, A. P. Sokolov, P. V. Sporyshev, K. E. Taylor, W.-C. Wang, R. T. Wetherald, Uncertainties in Carbon Dioxide Radiative Forcing in Atmospheric General Circulation Models. *Science* **262**, 1252–1255 (1993). https://doi.org/10.1126/science.262.5137.1252

14. W. D. Collins, V. Ramaswamy, M. D. Schwarzkopf, Y. Sun, R. W. Portmann, Q. Fu, S. E. B. Casanova, J. -L. Dufresne, D. W. Fillmore, P. M. Forster, V. Y. Galin, L. K. Gohar, W. J. Ingram, D. P. Kratz, M. -P. Lefebvre, J. Li, P. Marquet, V. Oinas, Y. Tsushima, T. Uchiyama, W. Y. Zhong, Radiative forcing by well-mixed greenhouse gases: Estimates from climate models in the Intergovernmental Panel on Climate Change (IPCC) Fourth Assessment Report (AR4). *J. Geophys. Res. Atmospheres*. **111**, D14317 (2006). https://doi.org/10.1029/2005JD006713

15. B. J. Soden, W. D. Collins, D. R. Feldman, Reducing uncertainties in climate models. *Science* **361**, 326–327 (2018). https://doi.org/10.1126/science.aau1864

16. N. Jeevanjee, J. T. Seeley, D. Paynter, S. Fueglistaler, An Analytical Model for Spatially Varying Clear-Sky CO_2 Forcing. *J. Climate* **34**(23), 9463–9480 (2021). https://doi.org/10.1175/JCLI-D-19-0756.1

17. K. E. Taylor, R. J. Stouffer, G. A. Meehl, An overview of CMIP5 and the experiment design. *B. Am. Meteorol. Soc.* **93**, 485–498 (2012). https://doi.org/10.1175/BAMS-D-11-00094.1

18. V. Eyring, S. Bony, G. A. Meehl, C. A. Senior, B. Stevens, R. J. Stouffer, K. E. Taylor, Overview of the Coupled Model Intercomparison Project Phase 6 (CMIP6) experimental design and organization. *Geosci. Model Dev.* **9**(5), 1937–1958 (2016). https://doi:10.5194/gmd-9-1937-2016

19. R. Pincus, S. A. Buehler, M. Brath, C. Crevoisier, O. Jamil, K. F. Evans, J. Manners, R. L. Menzel, E. J. Mlawer, D. Paynter, R. L. Pernak, Y. Tellier, Benchmark Calculations of Radiative Forcing by Greenhouse Gases. *J. Geophys. Res. Atmospheres* **125**, e2020JD033483 (2020). https://doi.org/10.1029/2020JD033483

20. X. Huang, X. Chen, C. Fan, S. Kato, N. Loeb, M. Bosilovich, S.-H. Ham, F. G. Rose, L. L. Strow, A synopsis of AIRS global-mean clear-sky radiance trends from 2003 to 2020. *J. Geophys. Res. Atmospheres* **127**, e2022JD037598 (2022). https://doi.org/10.1029/2022JD037598

21. G. Myhre, E. Highwood, K. P. Shine, F. Stordal, New estimates of radiative forcing due to well mixed greenhouse gases, *Geophys. Res. Lett.* **25**(14), 2715–2718 (1998). https://doi:10.1029/98GL01908

22. M. Etminan, G. Myhre, E. J. Highwood, K. P. Shine, Radiative forcing of carbon dioxide, methane, and nitrous oxide: A significant revision of the methane radiative forcing. *Geophys. Res. Lett.* **43**, 12,614–12,623 (2016). https://doi.org/10.1002/2016gl071930

23. B. Byrne, C. Goldblatt, Radiative forcing at high concentrations of well-mixed greenhouse gases. *Geophys. Res. Lett.* **41**, 152–160 (2014). https://doi.org/10.1002/2013GL058456

24. R. Caballero, M. Huber, State-dependent climate sensitivity in past warm climates and its implications for future climate projections. *Proc. Natl. Acad. Sci. U.S.A.* **110**, 14162–14167 (2013). https://doi.org/10.1073/pnas.1303365110

25. W. Zhong, J. D. Haigh, The greenhouse effect and carbon dioxide. *Weather* **68**(4), 100–105 (2013). https://doi.org/10.1002/wea.2072

26. J. T. Seeley, "[Convection, radiation, and climate: Fundamental mechanisms and impacts of a changing atmosphere]", thesis, University of California, Berkeley (2018). https://digitalassets.lib.berkeley.edu/etd/ucb/text/Seeley_berkeley_0028E_18385.pdf

27. Y. Huang, X. Tan, Y. Xia, Inhomogeneous radiative forcing of homogeneous greenhouse gases. *J. Geophys. Res. Atmospheres* ***121***, 2780–2789 (2016). https://doi.org/10.1002/2015JD024569

28. D. M. Romps, J. T. Seeley, J. P. Edman, Why the Forcing from Carbon Dioxide Scales as the Logarithm of Its Concentration. *J. Climate* **35**(13), 4027-4047 (2022). https://doi.org/10.1175/JCLI-D-21-0275.1

29. K. P. Shine, R. G. Derwent, D. J. Wuebbles, J.-J. Morcrette, "[Radiative forcing of climate]" in Climate change: The IPCC scientific assessment (Cambridge University Press, Cambridge, UK, 1990), pp. 41–68.

30. K. P. Shine, G. Myhre, The Spectral Nature of Stratospheric Temperature Adjustment and its Application to Halocarbon Radiative Forcing. *J. Adv. Model. Earth Syst.* **12**, e2019MS001951 (2020). https://doi.org/10.1029/2019MS001951

31. I. Mitevski, L. M. Polvani, C. Orbe, Asymmetric warming/cooling response to CO2 increase/decrease mainly due to non-logarithmic forcing, not feedbacks. *Geophys. Res. Lett.* **49**, e2021GL097133 (2022). https://doi.org/10.1029/2021GL097133

32. C. M. Bitz, L. M. Polvani, Antarctic climate response to stratospheric ozone depletion in a fine resolution ocean climate model. *Geophys. Res. Lett.* **39**, L20705 (2012). https://doi.org/10.1029/2012GL053393

33. E. A. Barnes, N. W. Barnes, L. M. Polvani, Delayed Southern Hemisphere climate change induced by stratospheric ozone recovery, as projected by the CMIP5 models. *J. Climate* **27**(2), 852–867 (2014). https://doi.org/10.1175/JCLI-D-13-00246.1

34. L. M. Polvani, M. Previdi, M. R. England, G. Chiodo, K. L. Smith, Substantial twentieth-century Arctic warming caused be ozone depleting substances. *Nat. Clim. Chang.* **10**, 130–133 (2020). https://doi.org/10.1038/s41558-019-0677-4

35. K. P. Shine, M. S. Bourqui, P. M. Forster, S. H. E. Hare, U. Langematz, P. Braesicke, V. Grewe, M. Ponater, C. Schnadt, C. A. Smith, J. D. Haigh, J. Austin, N. Butchart, D. T. Shindell, W. J. Randel, T. Nagashima, R. W. Portmann, S. Solomon, D. J. Seidel, J. Lanzante, S. Klein, V. Ramaswamy, M. D. Schwarzkopf, A comparison of model-simulated trends in stratospheric temperatures. *Q. J. R. Meteorol. Soc.* **129**, 1565–1588 (2003). https://doi.org/10.1256/qj.02.186

36. P. M. Forster, K. P. Shine, Radiative forcing and temperature trends from stratospheric ozone changes. *J. Geophys. Res. Atmospheres* ***102***, 10841–10855 (1997). https://doi.org/10.1029/96JD03510

37. A. C. Maycock, W. J. Randel, A. K. Steiner, A. Y. Karpechko, J. Christy, R. Saunders, D. W. J. Thompson, C. Zou, A. Chrysanthou, N. L. Abraham, H. Akiyoshi, A. T. Archibald, N. Butchart, M. Chipperfield, M. Dameris, M. Deushi, S. Dhomse, G. D. Genova, P. Jöckel, D. E. Kinnison, O. Kirner, F. Ladstädter, M. Michou, O. Morgenstern, F. O'Connor, L. Oman, G. Pitari, D. A. Plummer, L. E. Revell, E. Rozanov, A. Stenke, D. Visioni, Y. Yamashita, G. Zeng, Revisiting the Mystery of Recent Stratospheric Temperature Trends. *Geophys. Res. Lett.* ***45***, 9919–9933 (2018). https://doi.org/10.1029/2018GL078035

38. M. F. Stuecker, C. M. Bitz, K. C. Armour, C. Proistosescu, S. M. Kang, S. P. Xie, D. Kim, S. McGregor, W. Zhang, S. Zhao, W. Cai, Y. Dong, F. F. Jin, Polar amplification dominated by local forcing and feedbacks. *Nat. Clim. Chang.* **8**(12), 1076–1081 (2018). https://doi.org/10.1038/s41558-018-0339-y

39. Q. Fu, S. Solomon, H. A. Pahlavan, P. Lin, Observed changes in Brewer-Dobson circulation for 1980–2018. *Environ. Res. Lett.* **14**, 114026 (2019). https://doi.org/10.1088/1748-9326/ab4de7

40. P. J. Durack, P. J. Gleckler, F. W. Landerer, K. E. Taylor, Quantifying underestimates of long-term upper-ocean warming. *Nat. Clim. Chang.* **4**, 999–1005 (2014). https://doi.org/10.1038/nclimate2389

41. D. Roemmich, J. Church, J. Gilson, D. Monselesan, P. Sutton, S. Wijffels, Unabated planetary warming and its ocean structure since 2006. *Nat. Clim. Chang.* **5**, 240–245 (2015). https://doi.org/10.1038/nclimate2513

42. J. E. A. Marshall, J. Lakin, I. Troth, S. M. Wallace-Johnson, UV-B radiation was the Devonian-Carboniferous boundary terrestrial extinction kill mechanism. *Sci. Adv.* **6**, eaba0768 (2020). https://doi.org/10.1126/sciadv.aba0768

43. I. H. Campbell, C. M. Allen, Formation of supercontinents linked to increases in atmospheric oxygen. *Nat. Geosci.* **1**(8), 554 (2008). https://doi.org/10.1038/ngeo259

44. M. R. Warke, T. Di Rocco, A. L. Zerkle, A. Lepland, A. R. Prave, A. P. Martin, Y. Ueno, D. J. Condon, M. W. Claire, The Great Oxidation Event preceded a Paleoproterozoic "snowball Earth". *Proc. Natl. Acad. Sci. U.S.A.* **117**, 13314–13320 (2020). https://doi.org/10.1073/pnas.2003090117

45. J. G. Shepherd, (2009). "[Geoengineering the climate: Science, governance, and uncertainty]" In Working Group on Geoengineering the Climate (Royal Society, London, UK), pp. 1–98. https://royalsociety.org/topics-policy/publications/2009/geoengineering-climate/

46. A. Robock, Volcanic eruptions and climate. *Rev. Geophys.* **38**(2), 191–219 (2000). https://doi.org/10.1029/1998RG000054

47. D. T. Shindell, G. A. Schmidt, M. E. Mann, G. Faluvegi, Dynamic winter climate response to large tropical volcanic eruptions since 1600. *J. Geophys. Res. Atmospheres* **109**, D05104 (2004). https://doi.org/10.1029/2003JD004151

48. P. J. Rasch, S. Tilmes, R. P. Turco, A. Robock, L. Oman, C.-C. Chen, G. L. Stenchikov, R. R. Garcia, An overview of geoengineering of climate using stratospheric sulphate aerosols. *Philos. Trans. Royal Soc. A* **366**(1882), 4007–4037 (2008). https://doi.org/10.1098/rsta.2008.0131

49. A. J. Ferraro, E. J. Highwood, A. J. Charlton-Perez, Stratospheric heating by potential geoengineering aerosols, *Geophys. Res. Lett.* **38**, L24706 (2011). https://doi:10.1029/2011GL049761

50. B. Kravitz, A. Robock, D. T. Shindell, M. A. Miller, Sensitivity of stratospheric geoengineering with black carbon to aerosol size and altitude of injection, *J. Geophys. Res. Atmospheres* **117**, D09203 (2012). https://doi:10.1029/2011JD017341

51. M. G. Mlynczak, J. Yue, J. McCormack, R. S. Liebermann, N. J. Livesey, An observational gap at the edge of space, *Eos* **102** (2021). https://doi.org/10.1029/2021EO155494

52. S. Bony, M. J. Webb, C. S. Bretherton, S. A. Klein, P. Siebesma, G. Tselioudis, M. Zhang, CFMIP: Towards a better evaluation and understanding of clouds and cloud feedbacks in CMIP5 models. *CLIVAR Exchanges*, **56**, 20–22 (2011).

53. M. J. Webb, T. Andrews, A. Bodas-Salcedo, S. Bony, C. S. Bretherton, R. Chadwick, H. Chepfer, H. Douville, P. Good, J. E. Kay, S. A. Klein, R. Marchand, B. Medeiros, A. P. Siebesma, C. B. Skinner, B. Stevens, G. Tselioudis, Y. Tsushima, M. Watanabe, The Cloud Feedback Model Intercomparison Project (CFMIP) contribution to CMIP6. *Geosci. Model Dev.* **10**(1), 359–384 (2017). https://doi.org/10.5194/gmd-10-359-2017

54. R. Pincus, P. M. Forster, B. Stevens, The Radiative forcing model intercomparison project (RFMIP): experimental protocol for CMIP6. *Geosci. Model Dev.* **9**(9), 3447-3460 (2016). https://doi.org/10.5194/gmd-9-3447-2016

55. T. Andrews, C. J. Smith, G. Myhre, P. M. Forster, R. Chadwick, D. Ackerley, Effective radiative forcing in a GCM with fixed surface temperatures. *J. Geophys. Res. Atmospheres* **126**(4), e2020JD033880. (2021). https://doi.org/10.1029/2020jd033880

56. P. Good, T. Andrews, R. Chadwick, J.-L. Dufresne, J. M. Gregory, J. A. Lowe, N. Schaller, H. Shiogama, nonlinMIP contribution to CMIP6: model intercomparison project for non-linear mechanisms: physical basis, experimental design and analysis principles (v1.0). *Geosci. Model Dev.* **9**, 4019–4028. (2016). https://doi.org/10.5194/gmd-9-4019-2016

57. N. P. Gillett, H. Shiogama, B. Funke, G. Hegerl, R. Knutti, K. Matthes, B. D. Santer, D. Stone, C. Tebaldi, The Detection and Attribution Model intercomparison Project (DAMIP v1.0) contribution to CMIP6. *Geosci. Model Dev.* **9**, 3685–3697 (2016). https://doi.org/10.5194/gmd-9-3685-2016

58. D. M. Lawrence, G. C. Hurtt, A. Arneth, V. Brovkin, K. V. Calvin, A. D. Jones, C. D. Jones, P. J. Lawrence, N. de Noblet-Ducoudré, J. Pongratz, S. I. Seneviratne, The Land Use Model

Intercomparison Project (LUMIP) contribution to CMIP6: Rationale and experimental design. *Geosci. Model Dev.* **9**, 2973–2998 (2016). https://doi.org/10.5194/gmd-9-2973-2016

59. H. H. Aumann, M. T. Chahine, C. Gautier, M. D. Goldberg, E. Kalnay, L. M. McMillin, H. Revercomb, P. W. Rosenkranz, W. L. Smith, D. H. Staelin, L. L. Strow, J. Susskind, AIRS/AMSU/HSB on the Aqua mission: Design, science objectives, data products, and processing systems. *IEEE Trans. Geosci. Remote Sens.* **41**, 253–264 (2003). https://doi.org/10.1109/TGRS.2002.808356

60. H. T. Thrastarson, E. Manning, B. Kahn, E. J. Fetzer, Q. Yue, S. Wong, P. Kalmus, V. Payne, E. Olsen, R. C. Wilson, "AIRS/AMSU/HSB Version 7 Level 2 Product User Guide" (Jet Propulsion Laboratory, California Institute of Technology: Pasadena, CA, USA, 2020).

61. M. Schwartz, N. Livesey, W. Read, R. Fuller, MLS/Aura Level 3 Monthly Binned Temperature on Assorted Grids V004, NASA Goddard Earth Sciences Data and Information Services Center (2020); https://doi.org/10.5067/AURA/MLS/DATA/3221

62. M. Schwartz, N. Livesey, W. Read, R. Fuller, MLS/Aura Level 3 Monthly Binned Temperature on Assorted Grids V005, NASA Goddard Earth Sciences Data and Information Services Center (2021); https://doi.org/10.5067/Aura/MLS/DATA/3550

63. J. M. Russell III, M. G. Mlynczak, L. L. Gordley, J. J. Tansock Jr, R. W. Esplin, Overview of the SABER experiment and preliminary calibration results. *Proc. SPIE* **3756**, 277–288 (1999). https://doi.org/10.1117/12.366382

64. N. Smith, C. D. Barnet, Uncertainty characterization and propagation in the Community Long-term Infrared Microwave Combined Atmospheric Product System (CLIMCAPS). *Remote Sens.* **11**, 1227 (2019). https://doi.org/10.3390/rs11101227

65. H., Hersbach, Coauthors, The ERA5 global reanalysis. *Q. J. R. Meteorol. Soc.* **146**(730), 1999–2049 (2020). https://doi.org/10.1002/qj.3803

66. R. Gelaro, Coauthors, The Modern-Era Retrospective Analysis for Research and Applications, Version 2 (MERRA-2). *J. Climate* **30**(14), 5419–5454 (2017). https://doi.org/10.1175/JCLI-D-16-0758.1

67. M. Kanamitsu, W. Ebisuzaki, J. Woollen, S. K. Yang, J. J. Hnilo, M. Fiorino, G. L. Potter, NCEP-DOE AMIP-II reanalysis (R-2). *B. Am. Meteorol. Soc.* **83**(11), 1631–1644 (2002). https://doi.org/10.1175/bams-83-11-1631

68. J. M. Edwards, A. Slingo, Studies with a flexible new radiation code. I: Choosing a configuration for a large-scale model. *Q. J. R. Meteorol. Soc.* **122**(531), 689–719 (1996). https://doi.org/10.1002/qj.49712253107

69. J. Manners, J. M. Edwards, P. Hill, J.-C. Thelen, "SOCRATES (Suite Of Community RAdiative Transfer codes based on Edwards and Slingo) technical guide" (Met Office 2015).

70. S. A. Buehler, J. Mendrok, P. Eriksson, A. Perrin, R. Larsson, O. Lemke, ARTS, the atmospheric radiative transfer simulator — version 2.2, the planetary toolbox edition. *Geosci. Model Dev.* **11**(4), 1537–1556 (2018). https://doi.org/10.5194/gmd-11-1537-2018

71. D. D. Koll, T. W. Cronin, Earth's outgoing longwave radiation linear due to H2O greenhouse effect. *Proc. Natl. Acad. Sci. U.S.A.* **115**(41), 10293–10298 (2018). https://doi.org/10.1073/pnas.1809868115

72. M. Meinshausen, E. Vogel, A. Nauels, K. Lorbacher, N. Meinshausen, D. M. Etheridge, P. J. Fraser, S. A. Montzka, P. J. Rayner, C. M. Trudinger, P. B. Krummel, Historical greenhouse gas concentrations for climate modelling (CMIP6). *Geosci. Model Dev.* **10**(5), 2057–2116 (2017). https://doi.org/10.5194/gmd.10.2057.2017

73. T. Reichler, M. Dameris, R. Sausen, Determining the tropopause height from gridded data. *Geophys. Res. Lett.* **30**(20), 2042 (2003). https://doi.org/10.1029/2003GL018240

74. B. J. Soden, I. M. Held, R. Colman, K. M. Shell, J. T. Kiehl, C. A. Shields, Quantifying climate feedbacks using radiative kernels. *J. Climate* **21**, 3504–3520. (2008). https://doi.org/10.1175/2007JCLI2110.1

75. C. J. Smith, R. J. Kramer, A. Sima, The HadGEM3-GA7.1 radiative kernel: The importance of a well-resolved stratosphere. *Earth Syst. Sci. Data* **12**(3), 2157–2168. (2020). https://doi.org/10.5194/essd-12-2157-2020

Acknowledgments: We thank Drs. Adriana Sima, Chris Smith, and Pierre Nabat for clarifying CMIP standard online double-call methods, and Dr. Jacob Seeley for insightful discussions at the initial stage of this work. We also thank Drs. David Paynter and Pu Lin for their helpful comments.

Funding:

NOAA Award NA18OAR4310269 (HH, RJK, BJS)

NOAA Award NA21OAR4310351 (HH, BJS)

NASA Science of Terra, Aqua and Suomi-NPP grant 80NSSC21K1968 (RJK)

Author contributions:

Conceptualization: HH, RJK, BJS, NJ

Methodology: HH, RJK, BJS, NJ

Investigation: HH, RJK, BJS, NJ

Visualization: HH

Funding acquisition: RJK, BJS, NJ

Project administration: BJS

Supervision: BJS

Writing – original draft: HH, RJK, BJS

Writing – review & editing: HH, RJK, BJS, NJ

Competing interests: Authors declare that they have no competing interests.

Data and materials availability: The CMIP6 data are available at https://esgf-node.llnl.gov/search/cmip6/ while CMIP5 data are available at https://esgf-node.llnl.gov/projects/cmip5/. The CMIP6/5 models used in this work are listed in Tables S1–S5 in the Supplementary Materials. The AIRS temperature observations, Aura MLS retrievals, Aqua IR-only, SNPP, and NOAA-20 products produced using the CLIMCAPS algorithm, and the MERRA-2 reanalysis data are available at https://disc.gsfc.nasa.gov/datasets/. The processed level 2A SABER products can be found at https://data.gats-

inc.com/saber/custom/Temp_O3_H2O/v2.0/. The ERA5 reanalysis data are available at https://cds.climate.copernicus.eu/cdsapp#!/dataset/reanalysis-era5-pressure-levels-monthly-means?tab=overview. The NCEP-DOE Reanalysis 2 are available at https://psl.noaa.gov/data/gridded/data.ncep.reanalysis2.pressure.html. The benchmark radiative forcing values are obtained online (https://github.com/RobertPincus/rfmip-benchmark-paper-figures). SOCRATES is available from https://code.metoffice.gov.uk/trac/socrates but requires a free account from the UK Met Office to access the website. ARTS is available at https://www.radiativetransfer.org/getarts/ while PyRADS is available at https://github.com/danielkoll/PyRADS. Codes to produce the paper are available from the corresponding author upon request.

Supplementary Materials

Materials and Methods

Figs. S1 to S9

Tables S1 to S6

References (*52*–*75*)

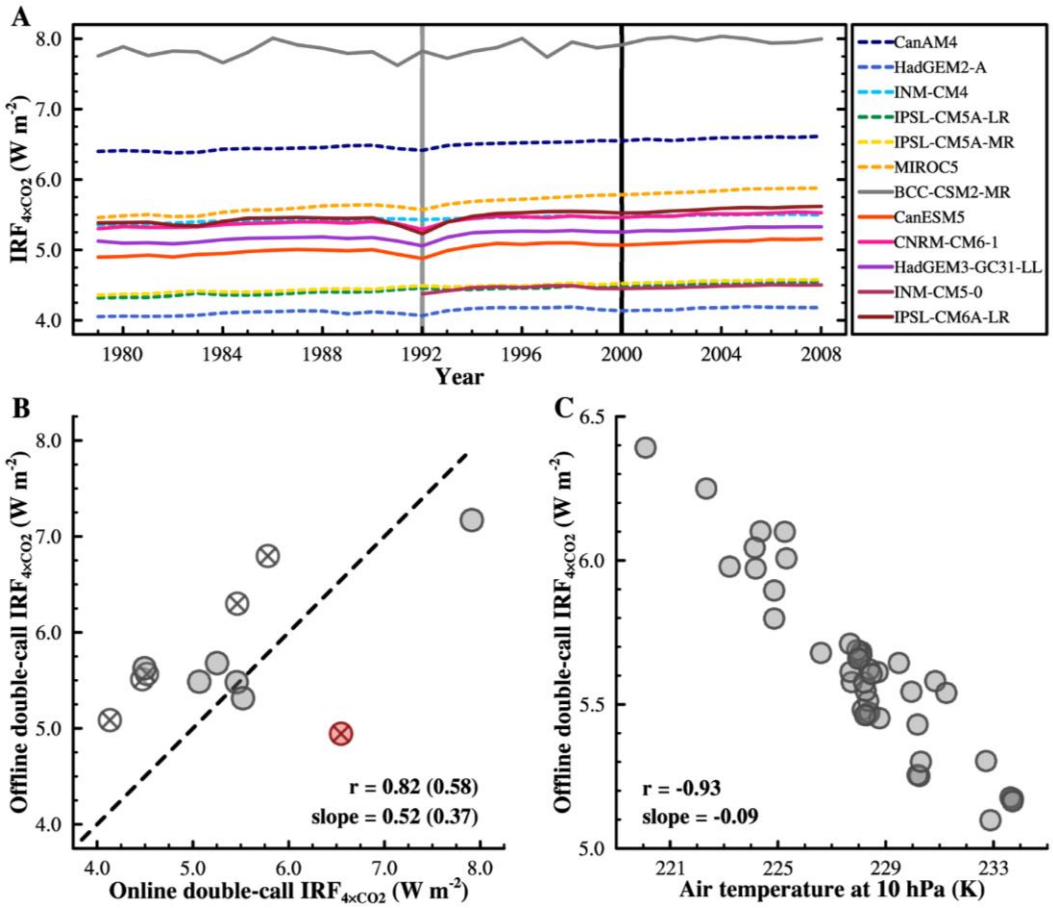

Fig. 1. The intermodel spread in $IRF_{4\times CO2}$ and its causes. (**A**) Time series of all available online double-call $IRF_{4\times CO2}$ with base-state from amip experiments for CMIP5/6 models. The black vertical reference line highlights the $IRF_{4\times CO2}$ values used in (B), while the gray one accentuates the brief declines in the magnitude of the $IRF_{4\times CO2}$ in the year 1992, following the eruption of Mount Pinatubo. (**B**) A comparison of the $IRF_{4\times CO2}$ in the year 2000 from the online and offline double-call calculations. The gray filled circles represent models from CMIP6, while the open circles with a cross inside show models from CMIP5. The red filled circle with a cross inside highlights the outlier model (i.e., CanAM4). Since the vertical IRF profile of CanAM4 shows an increase with height within the stratosphere [Fig. 3 of Chung and Soden (*10*)], it differs from the common expectation based on the negative lapse rate within the stratosphere. It is reasonable to exclude the results of the CanAM4 from the spread contribution analysis. The values in front of (in) parentheses shown in (B) are values calculated without (with) the outlier model CanAM4. (**C**) A scatterplot of global- and annual-mean air temperature at 10 hPa of each model in the year 2000 of the amip experiment versus its corresponding offline double-call $IRF_{4\times CO2}$.

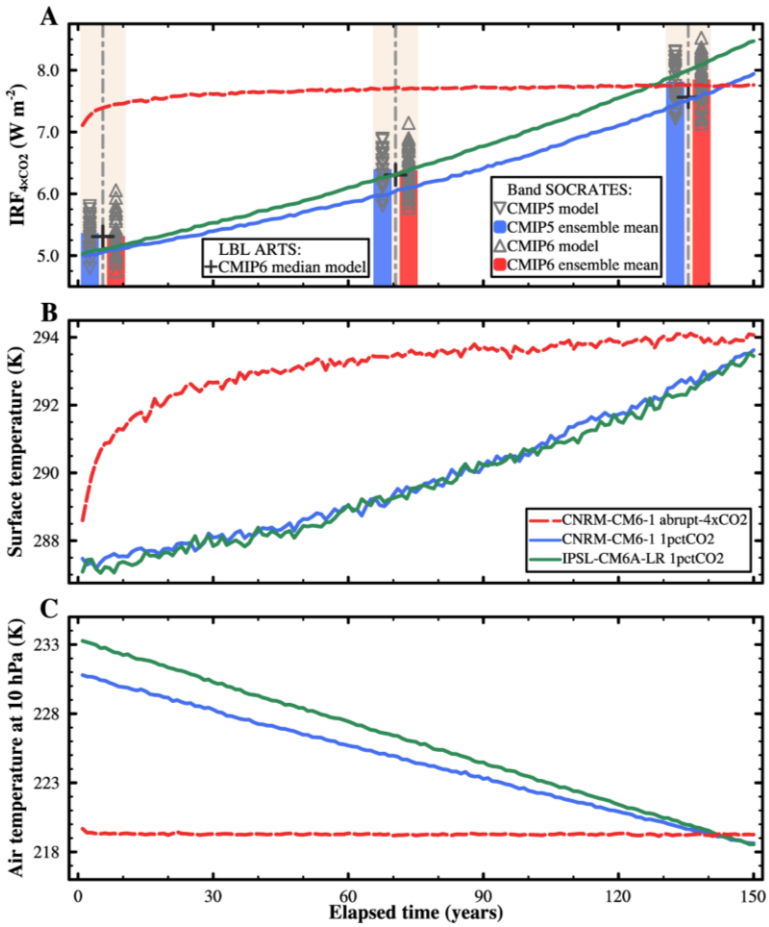

Fig. 2. The CO_2 IRF increases as the surface warms and the stratosphere cools. Time series of global- and annual-mean (**A**) online double-call $IRF_{4\times CO2}$, (**B**) surface temperature, and (**C**) air temperature at 10 hPa from models CNRM-CM6-1 and IPSL-CM6A-LR. Three highlighted time slices in (A) are years 1–10, 66–75, and 131–140. Overlaid gray triangles represent the global- and time-mean SOCRATES offline double-call $IRF_{4\times CO2}$ with corresponding atmospheric profiles of 1pctCO2 simulations from CMIP5/6 models. The black plus symbols show the global-mean ARTS offline double-call $IRF_{4\times CO2}$ with time-mean atmospheric profiles from the CMIP6 model, which has the median SOCRATES double-call $IRF_{4\times CO2}$ value. Similar results from another line-by-line model (PyRADs) are shown in Fig. S1. Note that the results in (A) represent IRF only and do not include any rapid adjustment. Rather the changes in IRF over time reflect the impact of the effects from prior CO_2 changes on the base-state which, in turn, amplifies the IRF that would result from a subsequent "hypothetical" quadrupling of CO_2.

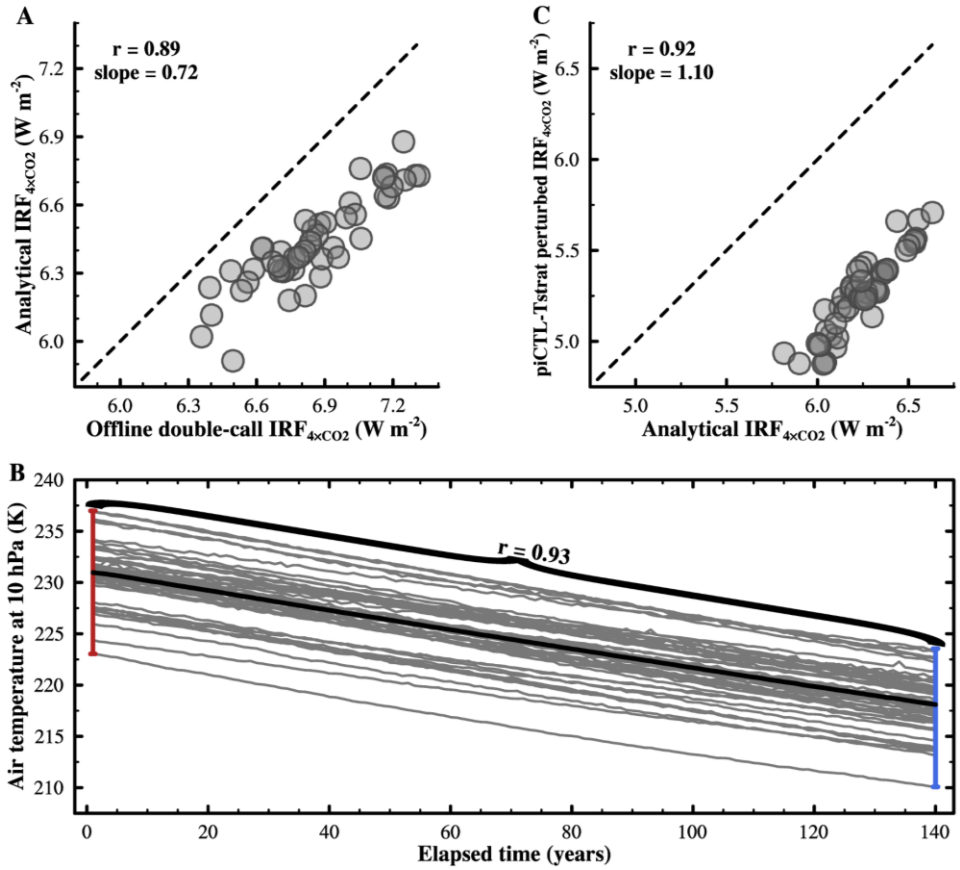

Fig. 3. Differences in initial stratospheric temperatures across models explain roughly half of the intermodel spread in $IRF_{4\times CO2}$, as shown using abrupt-4×CO2 experiments. (**A**) A comparison of global- and time-mean $IRF_{4\times CO2}$ in years 121-140 from the offline double-call and analytical model calculations with base-state from abrupt-4×CO2 experiments. The correlation between global- and time-mean $IRF_{4\times CO2}$ in every 10 of 150-year experiments from the offline double-call and the analytical model calculations ranges from 0.88 to 0.89. (**B**) Time series of global- and annual-mean 10 hPa air temperature under 1pctCO2 scenario from CMIP6 models. Each gray line in (B) represents the 10 hPa temperature evolution of a model, while the thick black line shows the multi-model ensemble mean. The curly bracket in (B) highlights the correlation between 10 hPa air temperature at years 1 and 140. (**C**) A comparison of the global- and time-mean original analytical $IRF_{4\times CO2}$ in years 2-11 and that obtained with perturbed stratospheric emission temperature from piControl runs (piCTL-Tstrat). The correlation between the global- and time-mean $IRF_{4\times CO2}$ from the original and piCTL-Tstrat perturbed calculations ranges from 0.90 to 0.92.

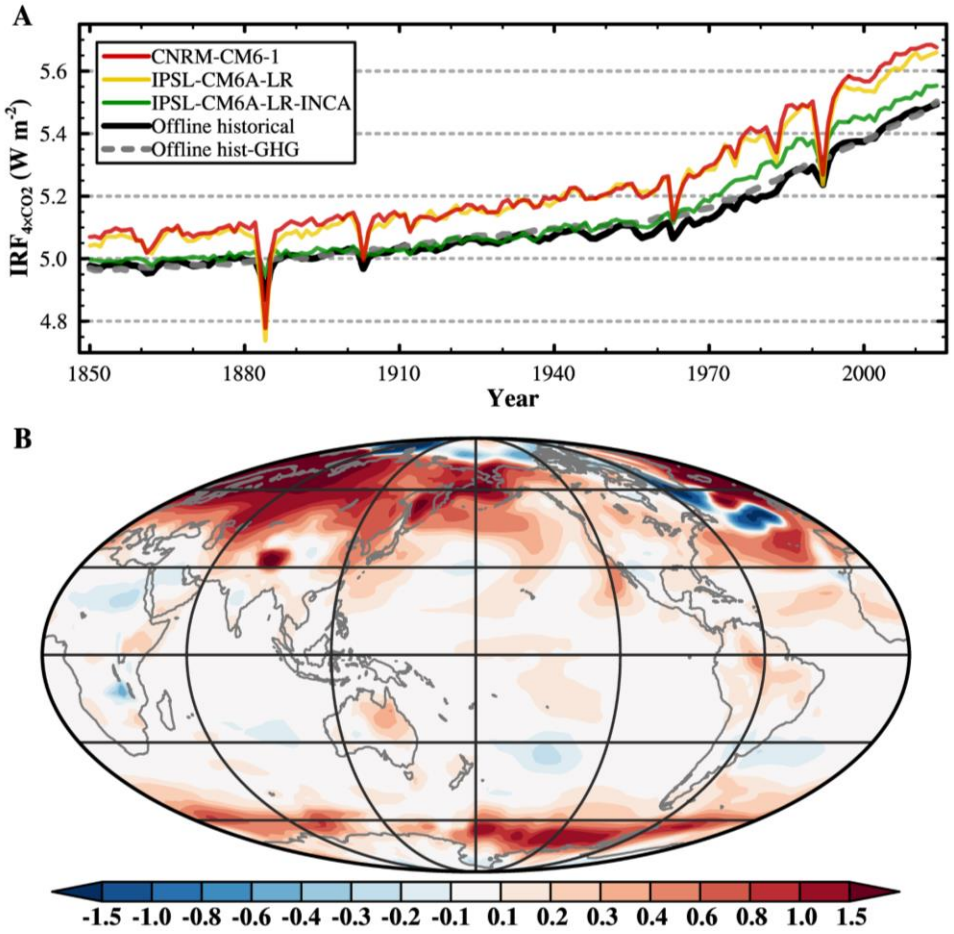

Fig. 4. Any forcing that perturbs the stratospheric temperature can further impact the climate by modulating the radiative forcing by CO_2. (A) Time series of three available online double-call $IRF_{4\times CO2}$ from CMIP6 historical simulations and the multi-model ensemble mean of corresponding offline double-call $IRF_{4\times CO2}$ for CMIP6 models with both historical and hist-GHG simulations. (**B**) The ensemble-mean map of the indirect surface warming effect of ozone depletion during the period 1985-2014.